SPE 159262

Laboratory Testing and Numerical Modelling of Fracture Propagation from Deviated Wells in Poorly Consolidated Formations

Ion Ispas, Robin A. Eve, Randall J. Hickman, Richard G. Keck, BP, Stephen M. Willson, BP now with Apache, Karen E. Olson, BP now with Southwestern Energy

This paper was prepared for presentation at the SPE Annual Technical Conference and Exhibition held in San Antonio, Texas, USA, 8-10 October 2012.

Abstract

This paper presents the results of an integrated laboratory and numerical modelling study on the effect of wellbore deviation and wellbore azimuth on fracture propagation in poorly consolidated sandstone formations. The goal of this project was to develop an understanding of how fractures would transition from single planar fractures to non-planar transverse fractures for fields in the deep-water Gulf of Mexico.

The foundation of this work was over 40 fracturing laboratory tests to measure fracture propagation geometries for a range of well deviations, differential horizontal stresses and rock strength. The samples tested were from three outcrops with unconfined compressive strength (UCS) values ranging from 300 – 1000 psi. For boreholes having low deviation angles and small differential stresses a vertical single planar fracture was created, aligned with the wellbore, as expected. As the well trajectory and stress contrast increased the fractures became more complex, with transverse turning fractures no-longer aligned with the wellbore.

These laboratory results were used to develop and calibrate a new fully-3D finite element model that predicts non-planar fracture growth. The model matches the details of the laboratory tests, including the transition from planar vertical to non-planar transverse fractures as the well deviation, azimuth and stress differentials increase. After initial model development and calibration was complete a model of a complex case was run before showing any experimental results to the modellers. The model successfully predicted the transverse non-planar results found in the laboratory; this gave us increased confidence in the model as a predictive tool.

This work has now been applied with excellent success to four deepwater fields. We have recommended changes in maximum well deviations, performed post-job analyses on wells that had high deviations, and have increased our understanding of the impact of layered formations on fracture growth in these fields.

Introduction

The impact of well trajectory relative to principal stress orientations on fracturing connectivity to wellbores has been extensively studied for hard rocks. Daneshy (1973) performed laboratory tests that raised awareness of the issue for the first time. Hallam and Last (1991) performed tests that demonstrated the impact of wellbore/fracture azimuth and deviation on fracture geometry and established an empirical relationship for field application. Weng (1992) developed a method to predict when multiple fractures would occur that also included the impact of horizontal stress anisotropy. These studies were applied to fields in the North Sea and Alaska that were well consolidated (having elastic moduli values of 1- 2 million psi) and where the horizontal stress differences were high enough to cause concern.

When the industry moved to frac-packs in the Gulf of Mexico in the early 1990's the issue of well deviation was thought not to be a major issue. This was based on the premise that unconsolidated formations had even lower moduli (0.1 - 0.5 million psi) and that the horizontal principal stress differences were relatively small. For example, at the Troika field (Porter et al, 2000), BP successfully frac-packed wells with deviations of over 60° with no discernible issues. The industry has now moved to deeper, higher pressure wells in sub-salt fields where the geology is considerably more complex than in the past. These

Miocene fields still need sand control completions but the horizontal stress variations are considerably larger than have been experienced in more benign settings.

The goal of the study was to understand how fracturing treatments behave in poorly consolidated sands for various wellbore configurations and in-situ stress conditions. Hydraulic fracturing laboratory tests were conducted using both small and large size blocks and a wide range of sandstone rock types ranging from poorly consolidated to harder rock. All the rock samples used were naturally formed (collected from outcrops) and are good analogues of the formations of interest. The type of tests included: (1) open hole with pre-perforated casing but no tunnels in the matrix; and (2) cased and perforated wellbore with tunnels in the matrix. A matrix of tests were performed with wellbore inclinations varying from 0 to 60° and wellbore azimuths from 0 to 90° relative to insitu stress directions that considered both isotropic and anisotropic stress states. The tested blocks considered both dry and saturated samples; and homogeneous and layered formations. The injected fracturing fluids had viscosities that varied from as low as 15 cP up to 2.5 million cP. Some tests were also monitored for acoustic emissions.

The following is a simple overview of some of the key issues that were addressed within this study.

Inclined Wellbores: in poorly consolidated formations inclined wellbores can cause problems due to restricted connectivity between the fracture and wellbore, with the potential for creating screen 'hot spots' that will not only result in an inefficient completion and convergent flow, but will also result in increased risk of screen failure. When the wellbore is deviated from the vertical it is desirable to initiate and propagate a fracture that runs longitudinally along the wellbore and covers the entire perforated interval. In addition, it is preferable to create a fracture that does not change direction from the point of initiation because this can generate lower widths and may lead to premature screen-outs.

Multiple Frac Initiation: failure to initiate a single fracture may also lead to the creation of non-planar geometry with multiple strands, re-orientations, T-shaped geometries and other complex systems. This is not a desirable scenario, as noted above.

Horizontal Stress Anisotropy: the relative magnitudes and orientations of in-situ stresses with respect to the wellbore are the primary controlling factors for the orientation of the hydraulic fracture created in both poorly- and highly-consolidated sands. Careful understanding and consideration of these aspects is essential in order to avoid fracture propagation in an undesired direction and to prevent the initiation of multiple fractures, which may result in adverse near-wellbore issues.

Plasticity: there have been several evaluations of the role that plasticity plays in the hydraulic fracturing process. Papanastasiou and Thiercelin (1993) and Papanastasiou (1997) investigated the influence of plastic deformation in hydraulic fracturing in cohesive materials using a coupled elasto-plastic finite element analysis; additionally, Agarwal and Sharma (2011) discuss the role that shear yielding plays in the fracturing of unconsolidated sands. Finally, a comprehensive description of recent developments in the modelling and simulation (both numerical and physical) of hydraulic fracturing in unconsolidated sands is included in Germanovich et al. (2012).

Experimental Conditions

Experimental Setup and Testing Procedures

The laboratory testing was conducted in both small and large polyaxial stress frames as shown in **Figures 1a** and **1b**. The stress frames make it possible to apply stresses in three principal directions: North-South (NS), East-West (EW), and Top-Bottom (TB). The stresses are generated using four flat-jacks for the horizontal directions and hydraulic cylinders in the vertical direction. The flat-jacks are steel bladders that are pressurized with fluid to expand and transmit loads to the sample within the stress frame. Volumetric strain measurements of the block during the hydraulic fracturing experiments, combined with acoustic emission monitoring, provide real-time indication of the fracture initiation, width and direction of propagation.

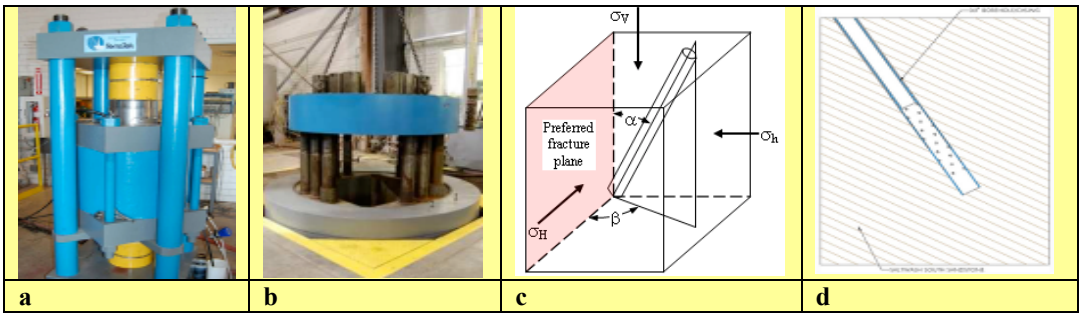

Figure 1 – Small (**a**) and large (**b**) polyaxial stress frames. Block sample geometry (**c, d**).

The small block tests were conducted on 11 × 11 × 15 inch samples. Boreholes were drilled in the samples with a 1.125 inch diameter borehole entering from the top of the sample. **Figure 1c** demonstrates that the boreholes were drilled at various desired inclinations *(α)* in reference to the vertical axis of the block and azimuth *(β)* which is the angle between the plane in which the wellbore is contained and the preferred fracture plane for each specific test. **Figure 1d** shows the borehole layout. The outside diameter of the casing used for the testing was stepped. The lower section had a 1.125 inch outer diameter in contact with the borehole wall with pre-perforated holes in various patterns. The upper portion of the casing had a 0.75 inch outside diameter. The annulus between the borehole and the casing was filled with epoxy to glue the casing firmly in place within the sample. In some cases a hydrostone filler was used to make up blocks to required dimensions.

The large block tests were conducted on 30 × 30 × 36 inch blocks. Each sample was prepared with a 1.50 inch diameter borehole entering from the top surface with a similar configuration to that used in the small block testing.

Rough cut sandstones were used to create the samples for all of the testing. The finished samples were formed with the bedding planes perpendicular to the vertical axis of the block.

During the fracturing tests the blocks were stressed with a pre-defined far-field overburden (σ_v), maximum horizontal (σ_H) and minimum horizontal (σ_h) stresses. After a block was placed under these specified far-field stress conditions a fracturing fluid was injected into the well casing until sufficient pressure was generated to create and propagate a fracture. A hydraulic pump was used with an in-line pressure intensifier. The intensifier was computer operated through volume displacement control. Continuous injection intensifier pumps were used to pressurise the flat-jacks under computer control to achieve, constant pressure/back-stress control. Electronic instrumentation was used to measure the applied stresses, injection pressures, injection rates and flat-jack displacements, and all of the data was recorded using a data acquisition system.

A typical injection rate for the 2.5 million cP viscosity fluid was 30 ml/min and for the cross-linked gel (1000 cP) 15 l/min (15000ml/min). The average fluid injection period for the high viscosity fluid was ~ 15-20 minutes and ~ 1-2 minutes for the cross-linked gel. After fracturing, the sample was removed from the test equipment and examined to determine the fracture morphology (shape, size, orientation, depth of leak-off, and extent of the fracture growth). Pressure and linear displacement transducers were used to measure block stresses, the wellbore pressure, and the volume of the injected fluid (Terratek, 2011).

Rock Types and Properties

As stated above, a wide range of sandstones rocks from poorly consolidated to hard rock were utilised, of which two rock types will be presented here - namely the Saltwash South and the Saltwash Red outcrop sandstones. The average formation and mechanical properties of the Saltwash South sandstone are: permeability (*k*) ~ 1,500 md, porosity (*ϕ*) ~ 31 %, unconfined compressive strength (*UCS*) ~ 300 psi, Young's Modulus (*E*) ~ 300,000 psi, and Poisson's Ratio (ν) ~ 0.35. The average formation and mechanical properties of the Saltwash Red sandstone are: permeability ~ 1,050 md, porosity ~ 24 %, *UCS* ~ 1,000 psi, Young's Modulus ~ 600,000 psi, and Poisson's Ratio ~ 0.24.

Fracturing Fluids

For the test results that are presented here a silicone polymer and a cross-linked gel were utilised. The viscosity of the silicon fluid was 0.1 to 2.5 million cP and that of the cross-linked gel is 1,000 cP. The high viscosity fluid was chosen to allow the tests to be correctly scaled for the block size and desired fracture propagation rate; see de Pater et al. (1994). The slower fracture propagation rate allows the fracture to reorient itself within the block only a short distance from the wellbore. The cross-linked gel was used to mimic realistic conditions and also to verify that tests using the silicone polymer were generating comparable results to what might actually happen under field operations. The silicone polymer fluid was dyed red and the cross-linked gel in blue in order to help identify the fractures during the post fracturing analysis and interpretation.

Experimental Results

Effect of Horizontal Stress Anisotropy

In this category a number of tests were performed using both small and large size Saltwash South samples. The testing conditions for each sample consisted of the same wellbore inclination ($\alpha = 60°$), the same wellbore azimuth ($\beta = 90°$), low effective vertical stress (σ_v = 1,200 psi), average maximum horizontal stress (σ_H = 780 psi), and a suite of horizontal stress ratios ($\sigma_H / \sigma_h = 1.0$, $\sigma_H / \sigma_h = 1.25$, $\sigma_H / \sigma_h = 1.5$, and $\sigma_H / \sigma_h = 3.0$). After testing each sample was carefully examined by external visual inspection followed by sample opening to reveal the fracture geometry which was subsequently photographed and catalogued. In some cases, smaller blocks or cylindrical shapes containing a portion of the fracture plane were cut and examined in a computerized tomography (CT) scanner to analyze the morphology of the fracture and its surrounding area. **Figure 2** shows some of the results of these tests. **Figure 2a** shows the test conducted at the highest stress ratio of $\sigma_H / \sigma_h = 3.0$

which produced transverse fractures. **Figure 2b** shows the same test conducted at a smaller stress ratio of $\sigma_H / \sigma_h = 1.25$; this produced a longitudinal (along the wellbore axis) fracture, perpendicular to the maximum horizontal stress, in the vicinity of the wellbore (region 1), which then subsequently reoriented to perpendicular to the minimum horizontal stress away from the wellbore (region 2). The test conducted at an isotropic stress state, $\sigma_H / \sigma_h = 1.0$, produced a vertical axial fracture as expected. The experimental results of the tests conducted in samples with a 60 degree wellbore inclination and the same wellbore azimuth in a non-preferred plane ($\alpha > 0$, $\beta > 0$) demonstrated that the fracture behaviour improved as the far-field horizontal stress ratio σ_H / σ_h decreased.

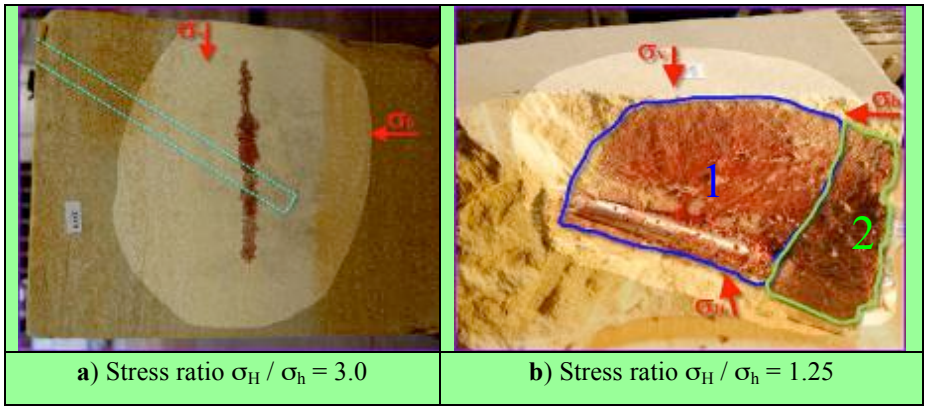

a) Stress ratio $\sigma_H / \sigma_h = 3.0$ | **b**) Stress ratio $\sigma_H / \sigma_h = 1.25$

Figure 2 – Experimental results from fracturing tests performed in Saltwash South sandstone (small size block) with identical wellbore orientation ($\alpha = 60°$, $\beta = 90°$), low stress magnitude ($\sigma_v = 1{,}200$ psi), but different far-field stress ratios: **a**) $\sigma_H / \sigma_h = 3.0$, and **b**) $\sigma_H / \sigma_h = 1.25$.

Effect of Wellbore Inclination with Stress Anisotropy

In this category tests were performed using both small and large size Saltwash South samples. The testing conditions for each sample consisted of different wellbore inclinations ($\alpha = 30°$, 45°, and 60°), the same wellbore azimuth ($\beta = 90°$), and anisotropic far-field stresses ($\sigma_v = 1{,}200$ psi, $\sigma_H = 780$ psi, $\sigma_h = 260$ psi). Examination of the experimental results from this sequence showed that for a wellbore inclination of $\alpha = 60°$ a transverse fracture was produced. The test with a wellbore inclination of $\alpha = 45°$ produced an inclined fracture that did not cover the entire perforated section and changed its orientation while propagating away from the wellbore. **Figure 3** shows the results of these tests. **Figures 3a** and **3b** show that the test with a wellbore inclination of $\alpha = 30°$ produced a penny-shaped fracture which was contained in a plane inclined at about 15° from the vertical but which subsequently changed its orientation as the fracture propagated away from the near-wellbore region. **Figure 3c** shows that the sample with a vertical wellbore orientation ($\alpha = 0°$) also produced a penny-shaped vertical axial fracture, as expected. The primary observation from this test is that for the case of an anisotropic far-field stress state and same wellbore azimuth in a non-preferred plane ($\beta > 0$), the fracture behaviour improves (becomes more like a conventional fracture expected from a vertical well) as the wellbore inclination decreases.

a) Deviation $\alpha = 30°$ | **b**) Deviation $\alpha = 30°$ | **c**) Deviation $\alpha = 0°$

Figure 3 - Experimental results of tests performed in Saltwash South sandstone with the same wellbore azimuth $\beta = 90°$, anisotropic far-field stresses ($\sigma_v = 1{,}200$ psi, $\sigma_H = 780$ psi, $\sigma_h = 260$ psi), and different wellbore inclinations: **a**) $\alpha = 30°$ (small size block), **b**) $\alpha = 30°$ (large size block) and **c**) $\alpha = 0°$.

Effect of Wellbore Azimuth with Stress Anisotropy

In this category, a series of tests were performed using small and large size Saltwash South samples. The conditions for these tests were: the same wellbore inclination (α = 60°), different wellbore azimuths (β = 0°, 45°, 60° and 90°), and fixed anisotropic far-field stresses (σ_v = 1,200 psi, σ_H = 780 psi, σ_h = 260 psi). **Figure 4a** shows the sample with a wellbore azimuth of β = 45° which produced a complex fracture inclined at ca. 15° from the vertical, which appears to change orientation away from the near wellbore region. **Figures 4b** and **4c** show that for wellbore azimuths of β = 60°and 90° a transverse fracture is produced. The test conducted through a wellbore aligned with the preferred fracturing plane (β = 0°) produced a penny-shaped vertical axial fracture. The conclusion for this category of tests is that for the same far-field stress state and the same non-zero wellbore inclination the fracture behaviour improved as the wellbore azimuth decreased. Also notable is the scalability of the test results when the same testing conditions and rock are used, but performed with different fracturing fluids - *silicon* in **Figure 4b** and *cross-linked gel* in **Figure 4c**.

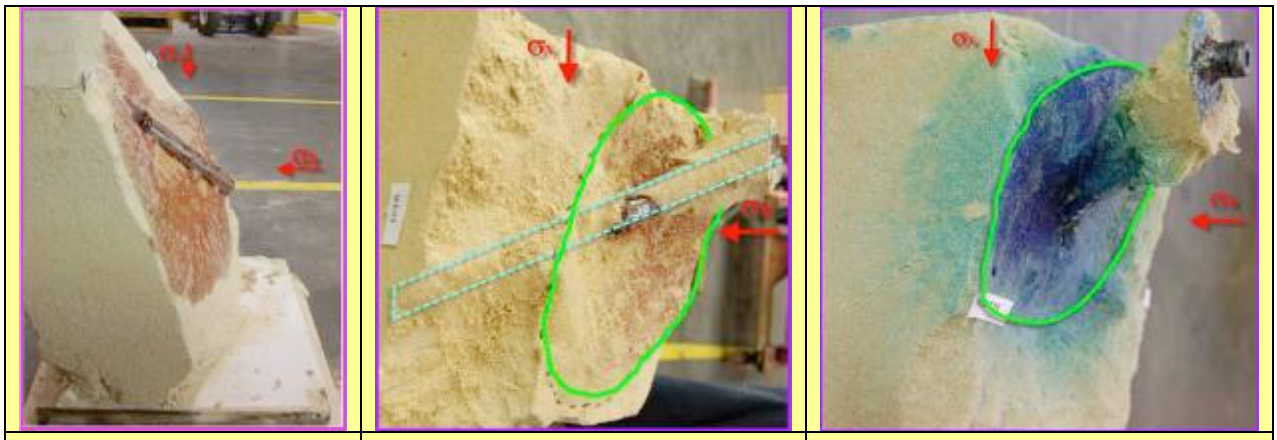

a) Azimuth β = 45° | **b**) Azimuth β = 60° | **c**) Azimuth β = 60°

Figure 4 - Experimental results of the suite of tests performed in Saltwash South sandstone with the same wellbore inclination (α = 60°) and far-field stress (σ_v = 1,200 psi, σ_H = 780 psi, σ_h = 260 psi) but with wellbore Azimuths of **a**) β = 45°, **b**) β = 60°, using silicon fracturing fluid, and **c**) β = 60°, using a cross-linked gel as the fracturing fluid.

Effect of Wellbore Inclination with Isotropic Horizontal Stresses

In this section we will examine the tests that were conducted using small size Saltwash South samples. The testing conditions for this suite of tests consisted of different wellbore inclinations (α = 30°, 45° and 60°) with the same wellbore azimuth (β = 0°) and an equal horizontal far-field stress state (σ_v = 1,200 psi, σ_H = 780 psi, σ_h = 780 psi). For all the tests in this category the results show that in a stress state with equal horizontal stresses the axial fractures initiate and propagate along the axis of the wellbore, covering the entire perforated length. **Figure 5** shows that the fracture behaviour does not change for the wellbore inclinations of 60° and 30°. **Figure 5a** shows that under equal far-field horizontal stress conditions it is possible to produce bi-wing fractures at different angles. **Figure 5b** shows the case in which one wing propagated from the casing in a direction approximately 15° to the west and the other fracture wing extended from the casing in a direction approximately 120° from the first wing. (Similar behaviour is observed by Germanovich *et al*, 2012).

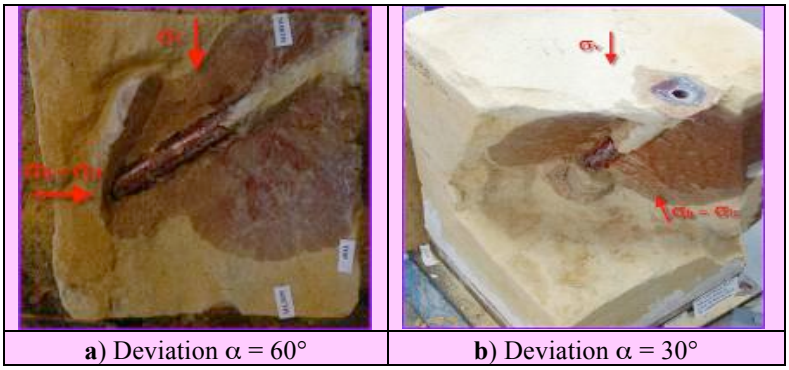

a) Deviation α = 60° | **b**) Deviation α = 30°

Figure 5 - Experimental results of the tests performed in Saltwash South sandstone with different wellbore inclinations: **a**) α = 60° and **b**) α = 30°, the same wellbore azimuth (β = 0°), and isotropic horizontal far-field stresses (σ_v = 1,200 psi, σ_H = 780 psi, σ_h = 780 psi).

Multiple Fractures

In this section the hydraulic fracturing test results conducted on a small size Saltwash Red sample are shown in **Figure 6**. The testing conditions for this test were: wellbore inclination $\alpha = 45°$, wellbore azimuth $\beta = 90°$, and anisotropic far-field stresses $\sigma_v = 2400$ psi, $\sigma_H = 1{,}560$ psi, $\sigma_h = 1{,}040$ psi. The experimental results show that multiple transverse fractures are produced. The fractures are parallel with each other and do not link up as they propagate away from the wellbore. If starter fractures fail to link up the interference among the fractures will cause some of them to close as they propagate away from the wellbore. If starter fractures fail to link up the interference among the fractures will cause some of them to close as they propagate away from their point of initiation.

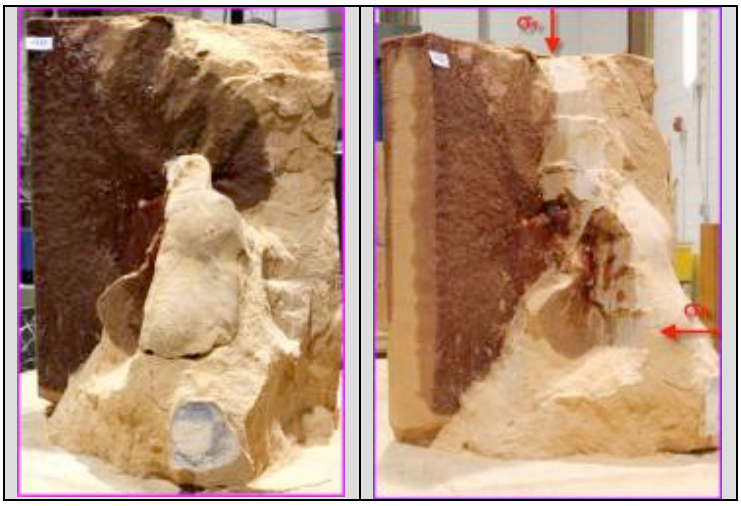

Figure 6 - Experimental results of the test performed in a Saltwash Red sandstone block with a wellbore inclination $\alpha = 45°$, azimuth $\beta = 90°$, and anisotropic far-field stress $\sigma_v = 2{,}400$ psi, $\sigma_H = 1{,}560$ psi, $\sigma_h = 1{,}040$ psi. Multiple transverse and parallel fractures are initiated in this configuration.

Fracturing Pressures

A typical graphic of the recorded fracturing pressure, the in-situ stress conditions and the cumulative injected fracturing fluid volume is illustrated in **Figure 7**. The pressure response progresses through three distinct phases: matrix injection (A), fracture propagation (B), and pressure fall-off (C), where P_{max} is the peak (breakdown) pressure, P_p is the post-peak fracturing propagation pressure, and P_{fo} is the falloff pressure after the pumps are stopped.

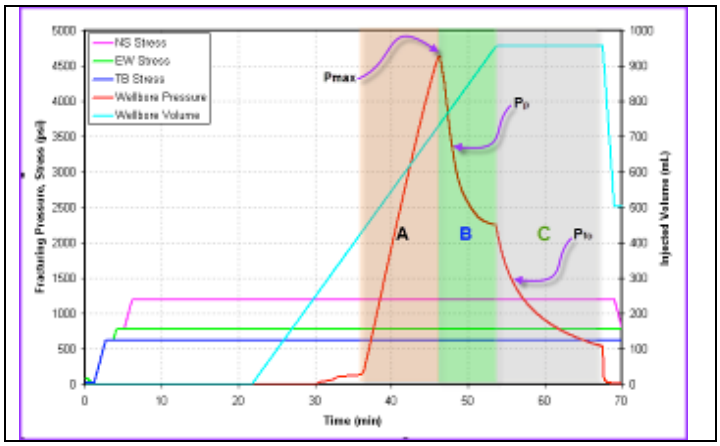

Figure 7 - Fracturing pressure, in-situ stress conditions and volume of fluid injected

Figure 8a illustrates the fracturing pressure behaviour (magnitude and shape) for a series of tests in Saltwash South samples with different wellbore inclinations but with the same wellbore azimuth and horizontal far-field stress ratio. The results for this category of tests indicate that when initiating a longitudinal (axial) fracture a lower breakdown pressure is recorded (lowest for this case, $P_{max} \sim 2{,}635$ psi: curve 3 in **Figure 8a**), whereas a higher breakdown pressure (highest in this case, $P_{max} \sim 3{,}620$ psi) is required to create a transverse fracture. The pressure behaviour for these two extremes of high deviation versus low deviation is also distinctive: from a sharp turn at the peak followed by a fast propagation for the case of a transverse fracture (high deviation, curve 1 in **Figure 8a**, shown in green color, having a small injected volume by the end of test**),** to a smooth

rollover at the delayed peak, followed by a slower propagation for an axial fracture (low deviation, curve 3 in **Figure 8a**, colored orange, having a much larger injected volume by the end of test).

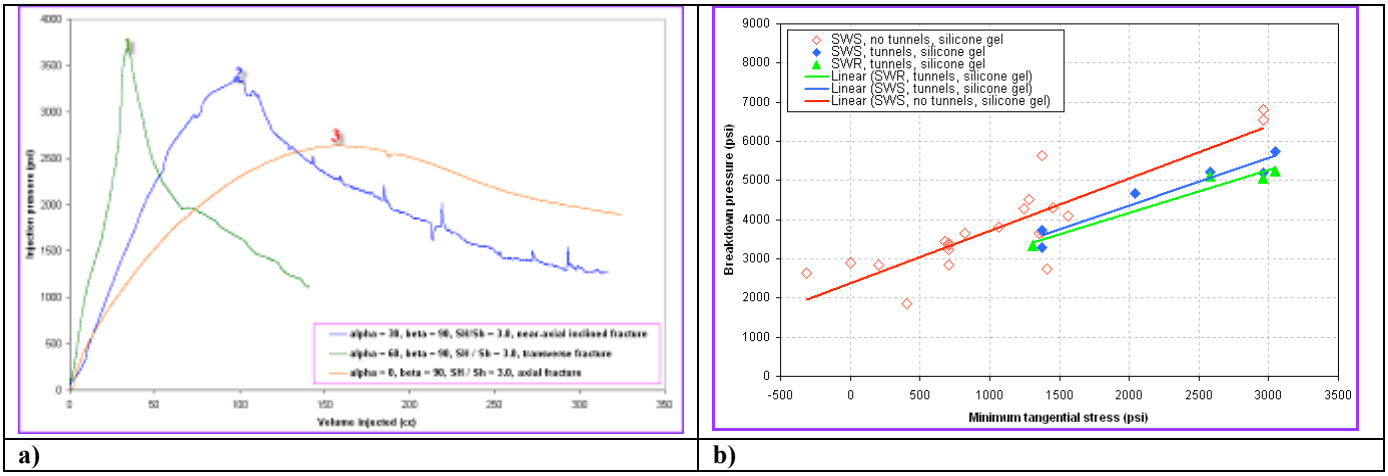

a) **b)**

Figure 8 - a) Injection pressure for different wellbore inclinations, the same wellbore azimuth, and the same horizontal far-field stress ratio **b**) Breakdown pressure as a function of the minimum tangential stress.

All three tests for which the pressure response is shown in **Figure 8a** were conducted with the same far field stress conditions (σ_v = 1,200 psi, σ_H = 780 psi, σ_h = 260 psi). The different wellbore orientations implemented in these three tests give rise to large differences in the near-wellbore stress state before injection commences. For example, test 1 has a minimum tangential stress of 1,375 psi; test 2 has a minimum tangential stress of 705 psi; and test 3 has a minimum tangential stress of - 315 psi. Hence the breakdown pressure for test 1 is ~ 2,245 psi greater than its reference (i.e. minimum tangential) stress; for test 2, ~ 2,620 psi greater than its reference stress; and for test 3, ~ 2,950 psi greater than its reference stress.

Figure 8b illustrates the recorded breakdown pressure magnitudes from several tests in both rock types (Saltwash South and Saltwash Red) as a function of the minimum tangential stress at the wellbore before injection commenced. The suite of tests was performed using two types of wellbore completions: (1) open hole with pre-perforated casing but no tunnels in the matrix, and (2) cased and perforated wellbore with tunnels in the matrix. The results in which perforation tunnels are present are displayed with solid symbols, and those in which the tunnels are absent are displayed with hollow symbols. The primary observations are that: (1) for the Saltwash South sandstone the use of perforation tunnels reduces the breakdown pressure by about 700 psi; and (2) the Saltwash Red sandstone, in which perforation tunnels are also present, exhibits slightly lower breakdown pressures than the Saltwash South sandstone under similar test conditions.

Numerical Modelling

The numerical modelling study of block fracturing tests presented here was performed by Rockfield Software Ltd. using the ELFEN finite element code. This code includes coupling between the mechanical and pore fluid behaviour, as well as contact interaction between the steel casing and the block material. The pore fluid coupling model is limited to single phase flow. The block material is represented with the proprietary SR3 material model. This model is described below and its formulation is included in the appendix, with further detail given by Crook et al. (2006).

The primary aim of the modelling work was to assess how well the geometry of created and propagated fractures in soft formation materials could be predicted. A preliminary study of fracture propagation in soft sands using a non-linear analysis indicated that shear damage rather than tensile failure is likely to dominate the development of localized highly conductive flow paths ("fractures") in "soft" sands. The approach used in modelling the block tests is based on determining localized mechanical damage rather than inserting discrete discontinuities, the mechanical damage being expressed as plastic strain.

SR3 – Rankine Material Constitutive Model

This elasto-plastic constitutive model is based on Critical State theory. It considers shear yield and compaction behaviour with shear softening and compaction hardening playing an important role in defining the material behaviour component. A Rankine tensile failure criterion is used in conjunction with the SR3 yield surface to account for tensile failure. A non-linear model of the elastic behaviour, appropriate for soft porous materials, is also incorporated. The SR3 yield surface is illustrated in **Figure 9**.

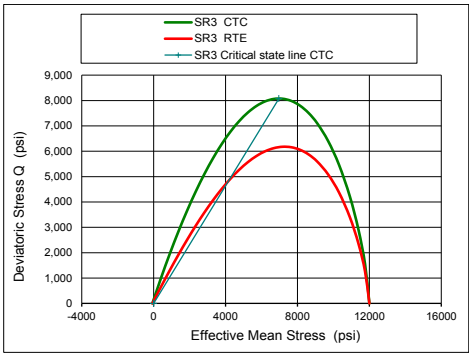

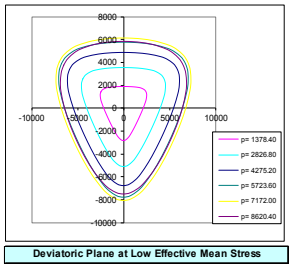

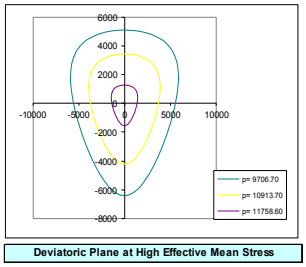

Note in these plots a compression is positive sign convention is used

Figure 9 - SR3 yield surface.

Tensile Failure

The Rankine tensile yield surface, or tensile cap, is a set of planes, each perpendicular to a principal stress. The model requires two parameters: the initial tensile strength T_0 and the fracture energy release rate G_f. The energy release rate defines the fall in tensile strength with increasing tensile plastic strain and is related to fracture toughness. In the analysis the tensile energy release is scaled to element size to limit mesh dependence.

Material Characterization

Characterization of the mechanical behaviour of the block materials (determination of input parameters for the SR3 material model) was based on standard confined triaxial compression (CTC), thick walled cylinder collapse (TWC) and in some cases hydrostatic triaxial compaction (HTC) and Brazilian tests. These tests were modelled to validate the material characterization. The element size used in the characterization process is used as a parameter in the energy-based regularization described by Crook et al. (2003), which is applied to avoid element size dependence.

Combined SR3 and Rankine Tensile Failure

Within each step of the analysis the elastic trial stress (predicted in absence of inelastic deformation) is first returned to the tensile yield surface; a plastic strain is generated to obtain this return, which also takes the reduction in tensile strength into account. The revised stress state is then checked against the SR3 shear yield surface and if necessary plastic shear strain and dilation develops as the stress is returned to the SR3 shear surface.

The tensile failure surface for a given Lode angle can be plotted as a straight line in the p - q plane. Limits corresponding to Lode angles of $\theta = 30°$ and $\theta = -30°$ (that is on CTC and RTE sections through the SR3 yield surface). The slope of the tensile failure line in the CTC and RTE sections are 3:1 and 3:2 respectively. This is illustrated in **Figure 10** for two cases: (**a**) with a high tensile intercept, and (**b**) with a low tensile intercept; plots of both full yield surface and low stress section are shown for each case. The tensile intercept relates to the material UCS as the fit to UCS data controls the position of the yield surface at low confinement; it is therefore also related to the cohesion of the material. The tensile surfaces are further inside the shear surfaces for the case with high UCS (**a**), hence in this case tensile failure is more likely than with low UCS (**b**).

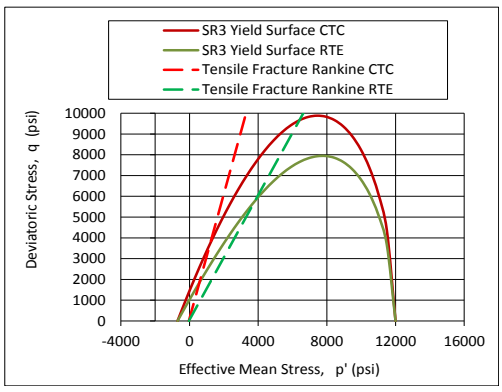

(a) T_0 = -40psi p_t=-700 psi (UCS = 3720psi)

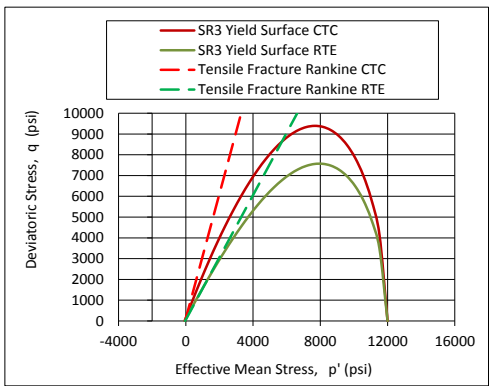

(b) T_0 = -40psi p_t=-70 psi (UCS = 225psi)

Figure 10 - Combined SR3 and Rankine yield surfaces.

Tensile and Shear Failure Stress Paths

An indication of a typical stress path recorded at a point on the plane of localized damage associated with the development of a fracture is also shown for each of the two cases in **Figure 11**; the Lode angle is typically close to 0° on these paths**.** The drop in mean effective stress on these stress paths is largely due to an increase in pore pressure as the result of matrix injection from the wellbore; near to the wellbore this pore pressure reflects the injection pressure.

In the case (**a**) with high UCS the stress path first meets the tensile yield surface, while in case (**b**) with low UCS the stress path first meets the shear yield surface; this mechanism is equivalent to that described by Agarwal and Sharma (2011). Tensile failure results in the development of a discrete fracture which generates a drop in the injection pressure and propagation of the fracture with fluid flow into the fracture.

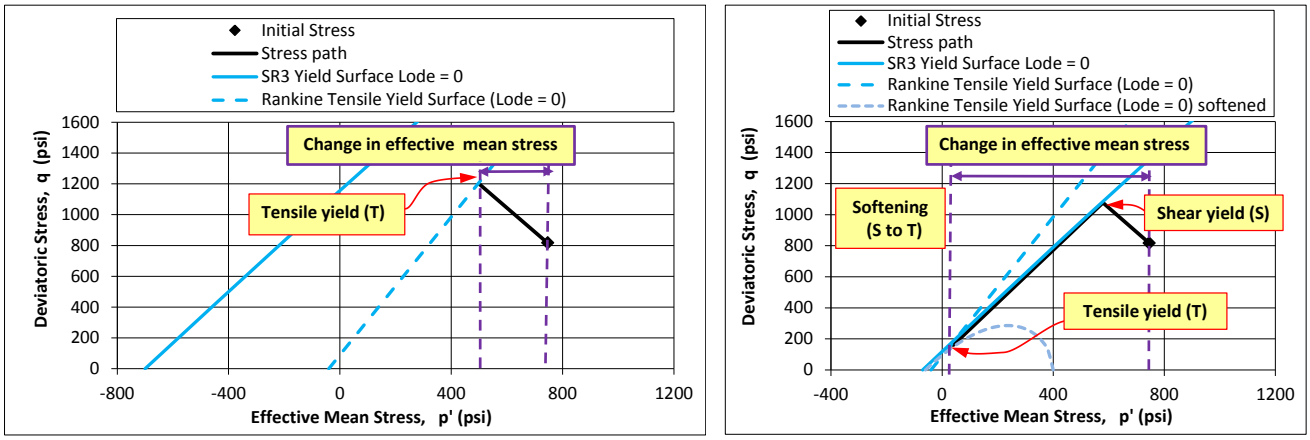

(a) T_0 = -40psi p_t=-700 psi (UCS = 3720psi) **(b)** T_0 = -40psi p_t=-70 psi (UCS = 225psi)

Figure 11 - Differences in stress paths to tensile fracture for high and low UCS materials.

In the case of shear yield, a localized dilated shear zone develops and the material softens. As injection pressure, and hence pore pressure, continues to rise the effective mean stress continues to fall. The stress path becomes limited by the softening (shrinking) of the shear yield surface. The increased porosity and hence permeability caused by shear dilation results in an increase in the conductivity of the localized shear plane; this alters the distribution of pore pressure in and around this plane. The local pressure gradients, which are dependent on the fluid viscosity and injection rate, alter the effective stress path. The stress path remains on the shear surface until the intersection with the tensile yield surface is reached at which point the weakened material in the shear damage zone parts in tension. The local transient pressure gradients generated with high viscosity fluids promote tensile failure while further shear is expected with low viscosity injection fluids. If the softening of the material is rapid the intersection with the tensile yield surface may not be reached before the mean effective stress becomes very low. This mechanism indicates one of the reasons why higher fracture initiation pressures may be expected in soft materials.

Numerical Block Models

The numerical block models include the block material with predrilled wellbore, the steel casing and, where necessary, a block of hydrostone filler. The modelled wellbore includes geometry defining the section contacting the perforated part of the casing - the injection pressure is applied over this section (the individual perforations in the casing are not modelled).

An unstructured mesh of tetrahedral elements was used. Typical meshes include approximately 270,000 elements. In cases with well azimuths of 0° or 90°, half block symmetry was used. Typical models are illustrated in **Figure 12**.

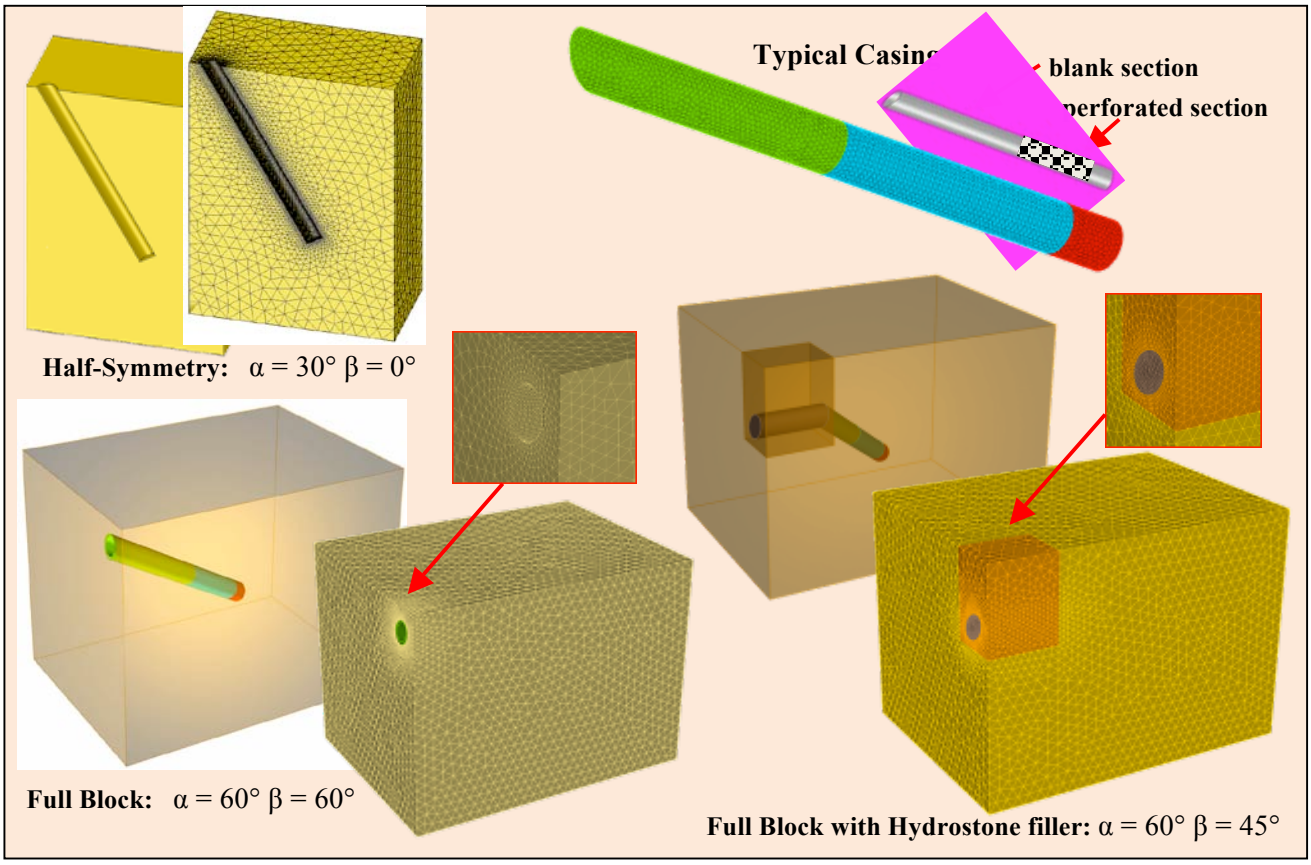

Figure 12 - Typical block model geometries and meshes.

Modelling Results

A variety of the laboratory tests undertaken were modelled numerically, but just a few selected examples are presented here. The results are provided as plots of 3D iso-surfaces of effective plastic strain. A small value of strain, typically 0.0005, is used to depict the boundary of the predicted damaged zone. These plots are compared with photographs of the equivalent laboratory tests in **Figures 13** to **17**.

The examples presented include:

- **Example 1**: A small block with α = 0° (vertical wellbore);this case provided an initial assessment of the model behaviour.
- **Example 2**: A large block with α = 30° β = 90°; this case was run with effective stress only (uncoupled). This case helped to confirm that the model boundary and scaling conditions do not have a significant influence on the results.
- **Example 3**: A small block with α = 30° β = 90°; this case shows moderate reorientation of the fracture after initiation along the perforated section of the wellbore.
- **Example 4**: A small block with α = 60° β = 90°; this case shows more significant reorientation of the fracture.
- **Example 5**: A small block with α = 60° β = 45°; this case shows fracture reorientation with a variation in well azimuth.

In all these examples the stress conditions are as follows: σ_v = 1,200 psi, σ_H = 780 psi, σ_h = 260 psi. The pairs of block faces on which these stresses are applied depends on the required well trajectory being simulated; the stresses applied on the Top and Bottom (TB), North and South (NS), and East and West (EW) faces have been provided for each example.

Example 1: Vertical well

In this example the model initially predicted localized shear damage development on the plane perpendicular to the minimum stress, then, at a later stage, tensile failure was predicted near the wellbore. As the model does not include the transition from shear damage to discrete fracture behaviour the final development of an open flow channel on the fracture is not captured.

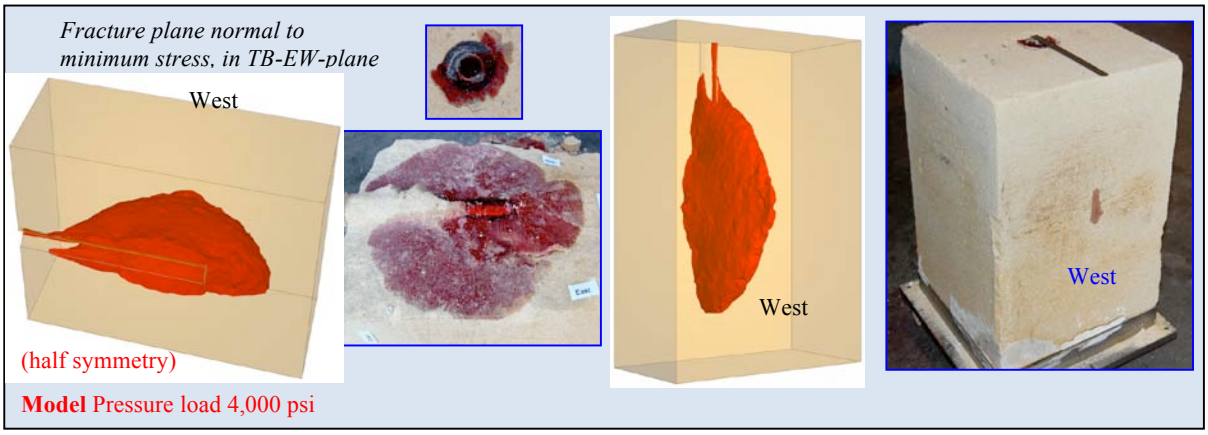

Figure 13 - Small Block (Vertical, σ_x [NS] = 260 psi, σ_y [EW] = 780 psi, σ_z [TB] = 1,200 psi).

Example 2: Large Block α = 30° β = 90° at low stress

This example was run at an early stage in the project at which time an effective stress analysis was used. The model predicts avery similar fracture geometry to that observed in the tests. The model predicts only shear damage which propagates to the state shown in **Figure 11**as the injection pressure reaches the breakdown pressure measured in the experiment..

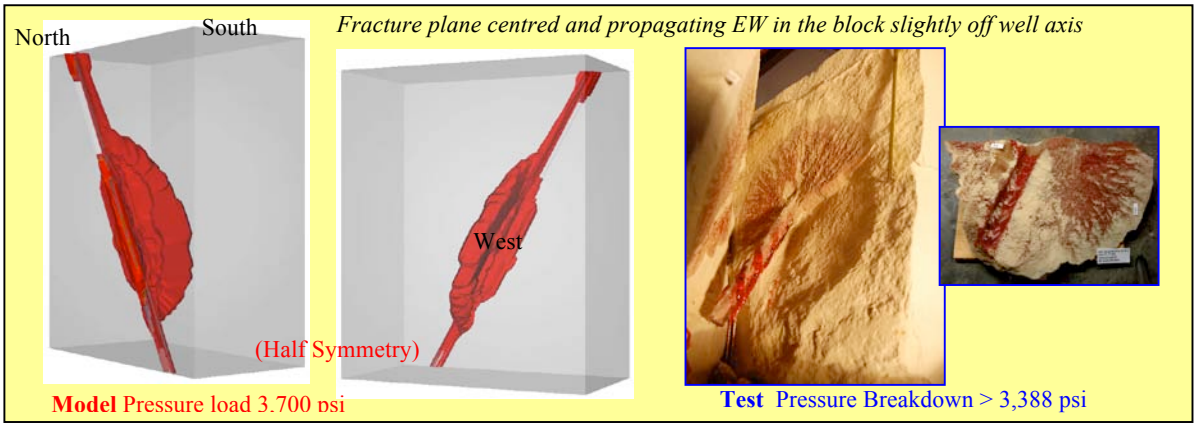

Figure 14 - Large Block (α=30° β=90°, σ_x [NS] = 260 psi, σ_y [EW] = 780 psi, σ_z [TB] = 1,200 psi).

Example 3: Small Block α = 30° β = 90°

In this example the predicted plane of the fracture is a very good match to that observed in the experimental test. However, in the test the fracture propagated asymmetrically (only to the west face of the block) while symmetry was assumed in the model.

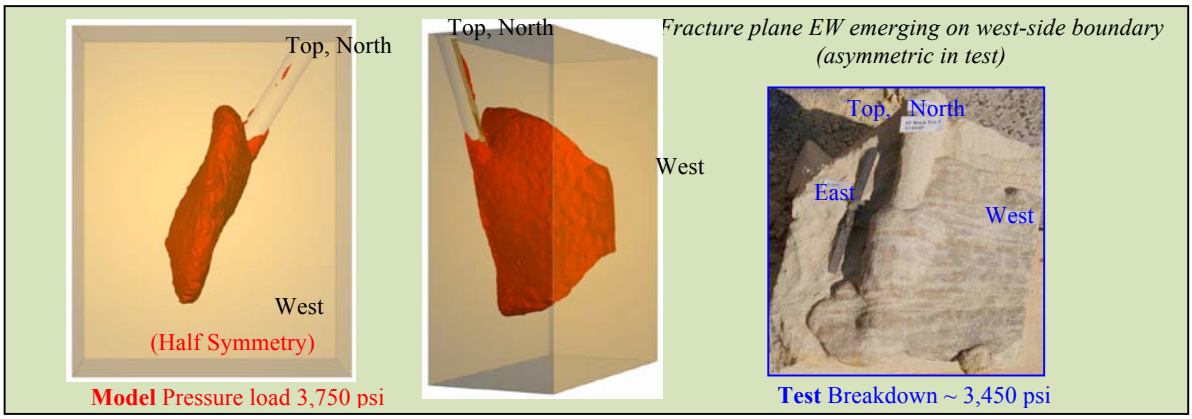

Figure 15 - Small Block (α = 30° β = 90°, σ_x [NS] = 260 psi, σ_y [EW] = 780 psi, σ_z [TB] = 1,200 psi).

Example 4 Small Block α = 60° β = 90°

In this example the general shape of the fracture plane predicted by the model is very similar to that observed in the test. It initiates over a slightly longer section of the wellbore than in the test, where the fracture propagates from the lower section of the perforated casing only. In the test a discrete fracture develops; however, it is not clear to what extent mechanical damage may have preceded the propagation of the fracture.

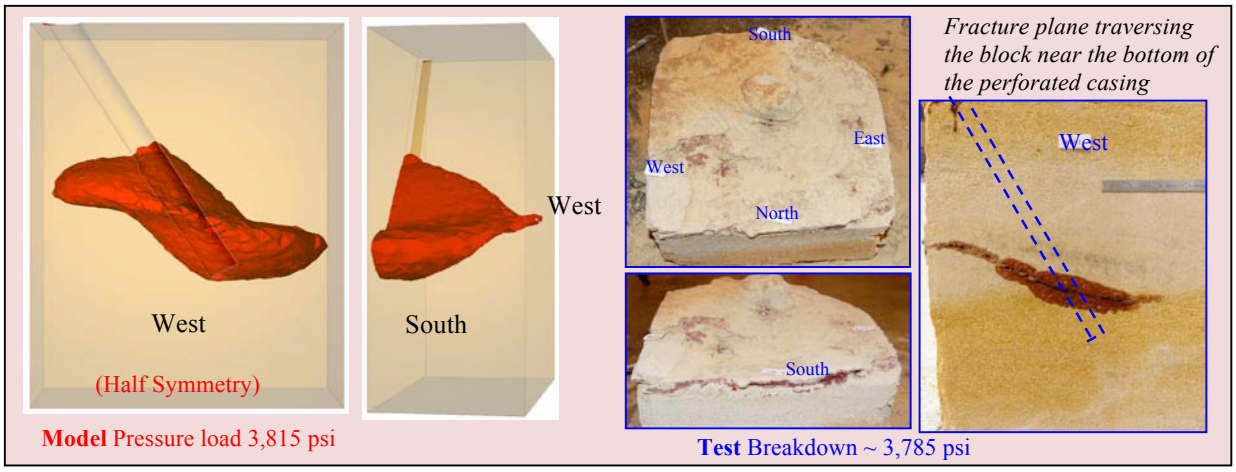

Figure 16 - Small Block Test (α = 60° β = 90°, σ_x [NS] = 1,200 psi, σ_y [EW] = 780 psi, σ_z [TB] = 260 psi).

Example 5: Small Block α = 60° β = 45°

In this example the fracture plane is captured with the model. In the test a narrow discrete fracture develops whereas the model predicts a wider damage zone. The width of the damage zone is exaggerated by the coarseness of the mesh and the absence of an inserted discrete fracture after shear damage has developed. While the energy dissipation within elements is regularized, the plastic strain is still smeared over the yielding elements.

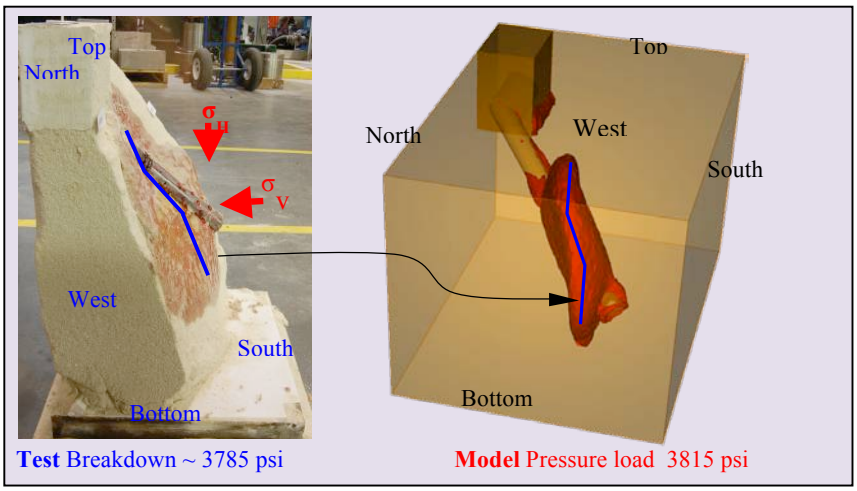

Figure 17 - Small Block Test (α = 60° β = 45°, σ_x [NS] = 1,200 psi, σ_y [EW] = 260 psi, σ_z [TB] = 780 psi)

Summary of Modelling Findings

Models based on predicting mechanical damage in the form of plastic strains generated mainly in shear has proved very effective in predicting fracture geometry for a range of well configurations and stress conditions. Some analyses of the stress paths show how a range of behaviours from the initiation and propagation of a purely tensile fracture to the generation of a localized plane of shear damage with associated dilation and hence enhanced conductivity can be obtained. The mode of behaviour is related to the UCS of the material and the initial state of stress. It is also influenced by an increased pore pressure ahead of the fracture tip, which in turn depends on the fluid rheology and injection rate.

The examples presented are for block tests where the length of the fractures is relatively small when compared with field applications. At field scale it becomes important to more accurately capture the influence of enhanced conductivity on planes of localized shear damage. Therefore in order to complete the model, the transition between a damage zone and a discrete flow plane/channel should also be included.

Conclusions

The aim of this work was to investigate, through an integrated laboratory and numerical modelling study, the effect of wellbore deviation and wellbore azimuth on fracture propagation and fracture morphology in poorly consolidated formations. The study shows that:

1. Hydraulic fracturing of poorly consolidated formations through a cased and perforated wellbore situated in a non-preferred plane ($\alpha > 0, \beta > 0$) produces fractures that improve their initiation behaviour (from transverse to axial) as the values of the wellbore inclination, the wellbore azimuth, and the far-field horizontal stress ratio decreases.
2. In isotropic horizontal stress conditions the fracture does not change propagation behaviour (it initiates, propagates, and remains axial along the wellbore axis) irrespective of the wellbore orientation (deviation and azimuth) with respect to the in-situ stress regime.
3. It is possible, but not desirable, to generate multiple and parallel en-echelon transverse fractures that will respectively close or fail to coalesce as they propagate away from the wellbore. Although seen in hard rock, it was initially uncertain as to whether these would be observed in the weaker rocks tested here. The testing has confirmed that this is the case.
4. Elevated and sharply decreasing post-breakdown fracturing pressures are associated with the creation of transverse fractures, whereas axial fractures exhibit a lower breakdown pressure.
5. The calibrated numerical modelling shows that in poorly-consolidated weakly cemented sandstones a shear failure mechanism precedes the development of a discrete conventional fracture. This helps to explain the elevated breakdown pressures that are typically observed in the field for this type of formation relative to harder rocks. This is considered to be an important result.
6. The shear damage predicted by the numerical model provides a reasonably reliable method of determining fracture geometry for a wide range of well trajectories and stress conditions. This provides confidence that the model can be used for predicting fracturing behaviour in this type of rock.

The overall understanding gained from this work has now been applied to four deepwater fields where, for example, recommendations for changes in maximum well deviations were made in order to optimise the hydraulic fracturing design. Post-job analysis of frac packed wells with wellbore inclinations of up to ~ 85° showed good agreement with our laboratory test results.

As indicated above, the type of tests performed thus far included (1) open hole with pre-perforated casing, but no tunnels in the matrix, and (2) cased and perforated wellbore with tunnels in the matrix, with wellbore inclinations from 0 to 60° and wellbore azimuths from 0 to 90°, dry and saturated samples, homogeneous and layered formations, and injection of fracturing fluids with viscosities from as low as 15 cP up to 2.5 million cP. Some tests were monitored for acoustic emissions. Finally, the tests were conducted under both isotropic and anisotropic stress conditions.

Additional experimental work is ongoing to further investigate fracturing initiation and propagation behaviour in other types of formations, incorporating various borehole configurations and in-situ stress conditions. Refinements to the numerical models are being implemented and the improved models are being used in further investigation of block tests, as well as in field scale applications.

Acknowledgments

We wish to acknowledge TerraTek for carefully carrying out a large number of experiments of high quality and Rockfield Ltd. for performing a significant number of numerical analysis, numerous colleagues for helpful discussions, and BP plc. for their permission to publish this paper.

Nomenclature

α = wellbore inclination from vertical
β = wellbore azimuth (measured away from the preferred fracture plane)
σ_v = effective vertical stress
σ_H = effective maximum horizontal stress
σ_h = effective minimum horizontal stress
d = diameter
l = length
ϕ = porosity
k = permeability
μ = viscosity
Pmax = breakdown pressure

Pp = post-breakdown injection pressure
Pfo = fall-off pressure
UCS = unconfined compressive strength
E = Young's modulus
ν = Poisson's ratio
A = a non-linear elastic model material constant
B = a non-linear elastic model material constant
β = material constant in definition of yield surface (only used in Appendix defining SR3 model)
β_0^{π} = material constant
β_1^{π} = material constant
E_{ref} = reference Young's Modulus for the a non-linear elastic model
ε_v^p = volumetric plastic strain
g = function that controls the shape of the yield surface in the deviatoric plane.
G_f = fracture energy release rate
J_3 = the third invariant of the deviatoric stress tensor
m = a non-linear elastic model material constant
n = a non-linear elastic model material constant
n = a material constant, elastic model and yield surface different constants
p = effective mean stress
p_c = pre-consolidation pressure or yield surface compressive hydrostatic axis intercept
p_t = yield surface tensile hydrostatic axis intercept
Φ = SR3 model yield surface
ψ = plastic flow potential
q = deviatoric stress
T_0 = initial tensile strength
r = a function of Lode angle
σ_3' = minimum effective principal stress
θ = Lode angle
υ_{low} and υ_{high} = limiting value of Poisson's ratio elastic model material
CTC = confined triaxial compression
RTE = reduced triaxial extension
HTC = hydrostatic triaxial compaction
TWC = thick walled cylinder
TB = top to bottom (in models -Z axis)
EW = east to west (in models Y axis)
NS = north to south (in models X axis)
LEFM = linear elastic fracture mechanics

References

Agarwal, K. and Sharma, M. M. 2011. Modeling Fracture Propagation in Unconsolidated Sands. ARMA 11-505, Presented at the 45th US Rock Mechanics / Geomechanics Symposium held in San Francisco, CA, June 26–29.

Crook, A.J.L . *et al.* 2003. Computational Modelling of the Localized Deformation Associated with Borehole Breakout in Quasi-Brittle Materials, Journal of Petroleum Science and Engineering 38, 177– 186

Crook, A.J.L. *et al.* 2006. Predictive Modelling of Structure Evolution in Sandbox Experiments, Journal of Structural Geology 28, 729–744.

Daneshy, A.A. 1973. A Study of Inclined Hydraulic Fractures, *SPE J.* (4) 61 - 68. SPE-4062.

de Pater, C.J. *et al* 1994. Experimental Verification of Dimensional Analysis for Hydraulic Fracturing, SPE 24994, Presented at the European Petroleum Conference, held in Cannes, France, Nov 16 -18.

Hallam, S.D. and Last, N.C. 1991. Geometry of Hydraulic Fractures from Modestly Deviated Wellbores, *J. Pet Tech* 1991, (6) 742 - 749 SPE 20656.

Germanovich, L.N. *et al*. 2012. Experimental Study of Hydraulic Fracturing in Unconsolidated Materials, SPE 151827, presented at the SPE International Symposium on Formation Damage Control in Lafayette, LA. Feb 15 -17.

Papanastasiou, P.1997. The Influence of Plasticity in Hydraulic Fracturing," Intl J Fracture, 84:61-79, Kluwer Academic Publishers, The Netherlands.

Papanastasiou, P. and Thiercelin, M.1993. Influence of Inelastic Rock Behaviour in Hydraulic Fracturing, 34th US Symp. Rock Mech., Madison, WI, June 27-30.

Porter, D.A. *et al.* 2000. Designing and Completing High-Rate Oil Producers in a Deepwater Unconsolidated Sand. SPE 58735, presented at the SPE International Symposium on Formation Damage Control in Lafayette, LA. Feb 23 -24.

Terratek, 2011. Block Fracturing Tests in Saltwash South Sandstone," BP Report, December 2011

Weng, X. 1993. Fracture Initiation from Deviated Wellbores. SPE 25967, presented at the 68th Annual Technical Conference and Exhibit held in Houston, TX, Oct 3 -6.

APPENDIX: SR3 – Rankine Material Constitutive Model

Elastic Behaviour

The Young's modulus and Poisson's ratio are dependent upon the minimum effective stress, σ_3':

Young's modulus

$$E = \{ E_{ref}\left[\frac{\sigma_3 + A}{B}\right]^n \text{ if } \sigma_3\text{' is compressive, } E_{ref}\left[\frac{A}{B}\right]^n \text{ if } \sigma_3\text{' is tensile}\}$$

where E_{ref} is a reference Young's modulus and A, B and n are material constants.

Poisson's ratio

$$\upsilon = \{ \upsilon_{low} + \left(\upsilon_{high} - \upsilon_{low}\right)\left(1 - e^{-m\sigma_3'}\right) \text{ if } \sigma_3\text{' is compressive, } \upsilon_{low} \text{ if } \sigma_3\text{' is tensile}\}$$

where υ_{low} and υ_{high} are limiting values, at zero and infinite values of σ_3' respectively, and m is a further material constant.

Shear Damage and Compaction

The SR3 model is a single surface rate independent non-associated plasticity constitutive model. The primary yield function is a smooth three-invariant surface that intersects the hydrostatic axis in both tension and compression and is defined by:

$$\Phi\left(\boldsymbol{\sigma}, \varepsilon_v^p\right) = g\left(\theta, p\right)q + (p - p_t)\tan\beta\left(\frac{p - p_c}{p_t - p_c}\right)^{1/n}$$

where p is the effective mean stress, q is the deviatoric stress, θ is the Lode angle, p_t is the tensile intercept of the yield surface with the hydrostatic axis, p_c is the pre-consolidation pressure or compressive intercept of the yield surface with the hydrostatic axis, β and n are material constants which define the shape of the yield surface in the p-q plane and $g(\theta, p)$ is a function that controls the shape of the yield function in the deviatoric plane. The evolution of the primary yield function is governed by the volumetric plastic strain ε_v^p via hardening-softening functions $p_c(\varepsilon_v^p)$ and $p_t(\varepsilon_v^p)$. The plastic strain is governed by a non-associated flow rule with plastic potential given by,

$$\Psi\left(\boldsymbol{\sigma}, \varepsilon_v^p\right) = g\left(\theta, p\right)q + (p - p_t)\tan\psi\left(\frac{p - p_c}{p_t - p_c}\right)^{1/n}$$

The deviatoric plane correction function $g(\theta, p)$ is defined as,

$$g(\theta,p)=\left[\frac{1}{1-\beta^{\pi}(p)}\left(1+\beta^{\pi}(p)\frac{r^3}{q^3}\right)\right]^{N}$$

where N^{π} is a material constant and β^{π} and r are defined as

$$\beta^{\pi}(p)=\beta_0^{\pi}\exp\left(\beta_1^{\pi}\,p\,\frac{p_c}{p_c^0}\right) \text{ and, } \mathrm{r} = 27\,J_3/2$$

where β_0^{π} and β_1^{π} are material constants; p_c^0 and p_c are the initial and current pre-consolidation pressure respectively; J_3 is the third invariant of the deviatoric stress tensor. The dependence of β^{π} on the effective mean stress enables the observed transition from the rounded-triangular yield surface at low mean stress to a circular yield surface at high mean stress.

The deviatoric plane correction is scaled so that the strength in triaxial compression directly corresponds to strength calibrated using compressive triaxial (CTC) tests and the strength is lower in reduced triaxial extension (RTE) tests; i.e.

RTE	$\theta=-30°$	$\sin 3\theta=-1$	$g=\left[\left(1+\beta^{\pi}\right)/\left(1-\beta^{\pi}\right)\right]^{N^{\pi}}$
	$\theta=0°$	$\sin 3\theta=0$	$g=\left[1/\left(1-\beta^{\pi}\right)\right]^{N^{\pi}}$
CTC	$\theta=30°$	$\sin 3\theta=1$	$g=1$